Ratio pyrometry of emulated firebrand streaks

James H. Baldwin, Peter B. Sunderland [*]

Dept. of Fire Protection Engineering, University of Maryland, College Park, MD, 20742, USA

ABSTRACT

Firebrands can dramatically increase the spread rates of large outdoor fires. Although much is known about other aspects of firebrand behavior, their temperatures are poorly understood. In particular, the temperatures of burning airborne firebrands have never been measured. In a novel configuration, airborne firebrand motion is emulated here by rotating a camera while imaging a tethered maple ember as a streaking ember. Ratio pyrometry is performed using a color digital camera calibrated with a blackbody furnace at 600–1200 °C. Over 1600 images of 55 stationary and streaking embers were recorded and analyzed. The same ember temperatures were obtained for stationary embers as for streaking embers with either a horizontal or a vertical axis of camera rotation. The mean ember temperatures were 918 ad 955 °C for 1 and 2 m/s wind velocities. These were independent of ember distance and velocity, but generally increased with time after ignition at a mean rate of 0.77 °C/s. The diagnostic has an estimated measurement uncertainty of ±20 °C and similar accuracy for stationary and streaking embers.

1. Introduction

Large outdoor fires, particularly in the wildland-urban interface, are responsible for tremendous losses of life and property [1–5]. Spot fires ignited by firebrands are a major mechanism by which wildland fires (and other large outdoor fires) propagate, and they ignite half of the structures burned in typical wildland fires [2,6]. Firebrands can be transported by wind and buoyancy up to 9 km [6]. They often accumulate in piles, enhancing the likelihood of spot fire ignitions [5,7].

There has been extensive research on firebrands, emphasizing their generation, morphology, transport, and ignition potential [5,8–12]. The measurement of firebrand temperatures is needed, but this has received relatively little attention [5]. Firebrand temperature is an essential parameter in the leading models of secondary ignition by firebrands. These temperatures are crucial because hotter firebrands are more likely to ignite a fuel bed, they reduce the ignition delay, and they decrease the critical firebrand mass for secondary ignition [5]. On the other hand, cool firebrands are more likely to extinguish before landing. Thus an improved understanding of firebrand temperatures could improve large outdoor fire prevention and response.

Ember temperatures have been measured using thermocouples [10, 13–15], but even fine thermocouples can quench the ember, suffer from poor thermal contact, and indicate temperatures 230 °C below actual [14]. No study to date has attempted to measure the temperatures of airborne firebrands with intrusive diagnostics.

Infrared (IR) imagers have been used for stationary ember pyrometry [6,10,15–17], but the cameras are expensive, have been limited to pixel counts below 1.5 megapixels, and can only measure temperatures of embers whose size is known or is larger in the image plane than several pixels. Furthermore they have relied on assumptions or thermocouple measurements in embers to account for the product of ember emissivity times ash transmittance. Most IR imagers do not filter more than one range of wavelengths, and thus cannot be used for ratio pyrometry, which precludes airborne firebrand pyrometry unless the size of the glowing region is known.

Ratio pyrometry of embers has been performed with digital color cameras [14,18]. These cameras are powerful and inexpensive, and their Bayer filter masks provide red, green, and blue pixel values at every pixel. Ratio pyrometry can be calibrated with a blackbody furnace [14, 18,19] or by imaging a glowing thermocouple [19], but it does not require thermocouple measurements in embers. Ratio pyrometry combined with grayscale pyrometry can yield hybrid pyrometry and $\varepsilon\tau$ in the visible range if this is independent of wavelength [14]. Ratio pyrometry has also accurately measured the temperature of soot [20], burning coal particles [21], and metal friction sparks [19].

For airborne firebrands, ratio pyrometry has three main advantages over single-band pyrometry. First, the ember emissivity times ash transmittance need not be known. Indeed, the assumption that emissivity is independent of the pyrometer wavelengths is ubiquitous in ratio pyrometry of solids [14,18,19,21]. Second, the firebrand dwell time (i.

---

* Corresponding author. Dept. of Fire Protection Engineering, University of Maryland, 3104 J.M. Patterson Building, College Park, MD, 20742, USA.
  E-mail address: pbs@umd.edu (P.B. Sunderland).

Fig. 1. Top-view schematic for stationary camera tests and tests with a vertical axis of camera rotation. The white + symbol and arrow denote the rotation axis and direction.

e., the elapsed time during which a pixel is illuminated) need not be known. Third, the firebrand image size need not be known even when it is comparable to one pixel. On the other hand, the signal-to-noise ratio for single-band pyrometry has been found to be a factor of 18 higher than for ratio pyrometry [14].

Pyrometry of burning airborne firebrands has never been performed. Ratio pyrometry was performed for airborne metal spheres and friction sparks [19], but these were not wood embers and the measured temperatures were only independently verified in a small number of tests. Temperature measurements of airborne metal spheres with a thermal imager were discussed by Ref. [22].

Firebrand pyrometry is demonstrated here using streaking embers for the first time. These are stationary tethered embers, with known temperatures, that are imaged as streaks while rotating the camera. They allow independent control of the wind velocity and the ember velocity, which is not possible with airborne firebrands. The resulting streak images are identical to those that would be recorded by a stationary camera observing a non-tumbling airborne ember of the same temperature, size, distance, and velocity relative to the camera.

2. Experimental

A schematic of the apparatus is shown in Fig. 1. The embers were dry round maple rods with a diameter of 6 mm, a length of 25 mm, and a 3.2 mm hole on center [14]. Their masses were 360 ± 40 mg. They were supported with two 225 μm Nichrome wires passing through the hole. Similar tethered embers have been considered before [8,14,16]. A steady incident wind velocity, V_{wind} (1 or 2 m/s), with an estimated uncertainty of ± 0.1 m/s, was provided by a variable-speed 100 mm computer case fan positioned higher than the ember and between it and the camera. The wind velocity experienced by an airborne firebrand is generally its terminal velocity [8], which, for these rods, is 8 m/s for burning rods [8] and 12 m/s for non-reacting rods [23]. The wind velocities used for the present tests, 1 and 2 m/s, were relatively low to increase the ember smolder durations.

Ignition was accomplished by impinging a 50 mm butane laminar diffusion flame across the bottom of the rod for 8 s. Flaming combustion ceased a few seconds later. Time zero was defined as the onset of flame

impingement. The pyrometry commenced when the entire surface began smoldering, at about 35 s after ignition, and terminated when the first large pieces of the ember detached.

Color pyrometry was performed using a Sony DSC-RX10 III camera, with a 13.2×8.9 mm Exmor RS CMOS sensor, pixel dimensions of 5472×3648, and a bit depth of 14 in each color plane [14]. The lens was a Zeiss Vario-Sonnar T* 24–600 mm with available f-numbers of $f = 2.4–4$, but all images were recorded at a focal length of 24 mm and $f = 2.4$. No external optical filters were used.

Images were captured in RAW format and converted to 16-bit TIFF format using dcraw [14,24]. Fixed channel multipliers were used for the dcraw white balancing, and bilinear interpolation demosaicing [25] was applied. Normalized pixel values were defined as

$$NI_i = (I_i - I_{i,DC}) f^2 / t \ ISO, \tag{1}$$

where I is pixel value; DC is the dark-current pixel value absent illumination, a function of t; i denotes R, G, or B; t is exposure time; and ISO is the International Organization for Standardization camera gain.

The camera was calibrated by imaging a blackbody furnace at various temperatures, f, ISO, and t. The blackbody was an Oriel 67032 with an aperture of 25.4 mm, a maximum temperature of 1200 °C, and an emissivity of $\varepsilon = 0.99 \pm 0.01$ [14]. Calibration images were recorded at temperatures of 600–1200 °C and at distances of 4.2–200 cm [26]. The exposure times were selected such that the red and green pixel values were high without approaching saturation. This confirmed the calibration of [14] for a different camera of the same model. The calibration yielded a monotonic relationship between blackbody temperature and NI_G/NI_R. The blue pixel values were too low to be useful.

The spectral emissive power of a point on an ember is

$$E_\lambda = \varepsilon \ \tau \ C_1 / \lambda^5 \ [\ \exp (C_2 / \lambda \ T) - 1 \ ], \tag{2}$$

where ε is ember emissivity; τ is ash transmittance; C_1 and C_2 are the first and second radiation constants (3.742×10^{-16} W-m^2 and 0.01439 m-K); λ is wavelength; and T is temperature. It is assumed here that $\varepsilon\tau$ for embers does not vary with wavelength between red and green.

For each pixel in each image, NI_G/NI_R was converted to pixel temperature using the blackbody calibration. Two noise filtering steps were then applied, as optimized by Ref. [14]. In the first step, pixels approaching saturation (a pixel value of 65,535), pixels with green pixel values below 100, and pixels with raw temperatures outside the calibration range (600–1200 °C) were assigned null temperatures (i.e., $T = -1 \times 10^{99}$ °C). In the second step, null temperatures were assigned where the majority of pixel temperatures in the surrounding 7×7 pixel region were null after the first step. The image analysis was performed using Matlab.

Tests without camera rotation recorded *stationary ember* images at 1 Hz. For each such image, the *image temperature* is defined as the mean of the non-null temperatures in the image. The mean of all the image temperatures for an ember is defined as the *ember temperature*. The standard deviation of the image temperatures was also found. As summarized in Table 1, 406 images of 15 stationary embers were recorded and analyzed at various *OID* (object-to-image distance) and V_{wind}.

Table 1
Summary of the pyrometry tests performed.

rotation axis	OID, m	V_{em}, m/s	V_{wind}, m/s	no. embers	no. images	mean T, °C[a]	stdev T, °C[b]
none	0.375–3	0	1	12	347	916	19
	0.375–1.5	0	2	3	59	964	17
horizontal	0.375–1.5	2–12	1	4	194	915	19
	0375–1.5	2–12	2	4	105	930	30
vertical	0.375–1.5	2–16	1	15	467	920	27
	0.375–1.5	2–16	2	17	432	957	24
TOTAL				55	1604		

[a] The mean of the images in this row.
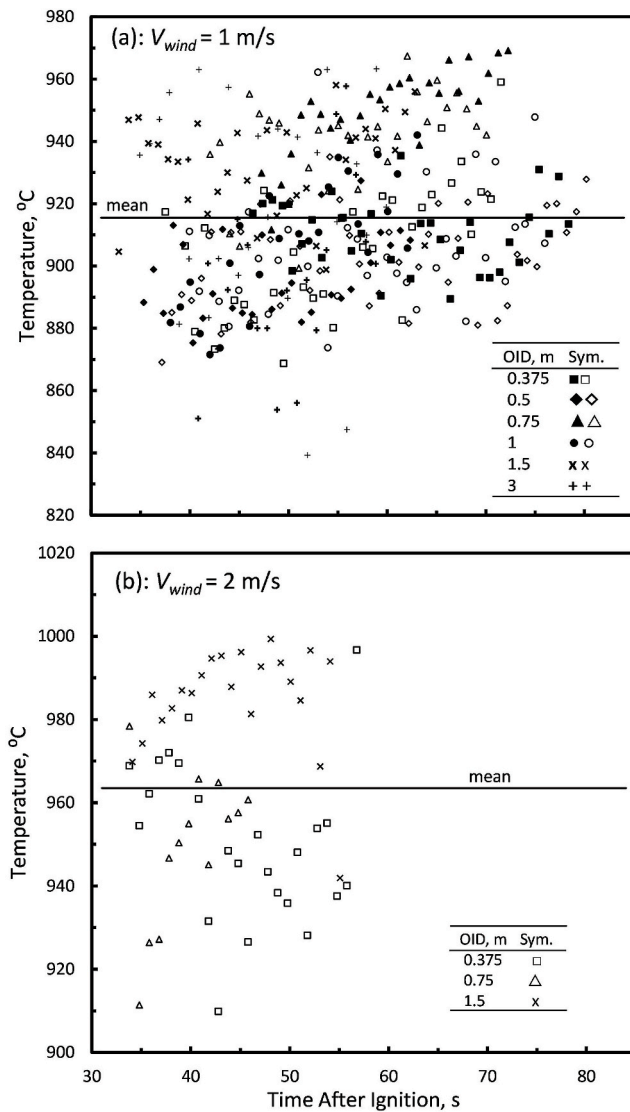[b] The mean of the standard deviation for each ember in this row.

Fig. 2. Stationary ember image temperature versus time after ignition for (a) 12 embers with $V_{wind} = 1$ m/s and (b) 3 embers with $V_{wind} = 2$ m/s. The conditions were $ISO = 100$ and $t = 1.56$ ms. Each point represents a single image.

Fig. 3. Stationary ember temperature and $\varepsilon\tau$ in the visible versus OID for 12 embers with $V_{wind} = 1$ m/s. Each point represents one ember, averaged over all its recorded times. Lines denote the means of the points shown.

For both the stationary and streaking embers, the image temperatures have an estimated uncertainty of ± 20 °C. The largest factor in this uncertainty is the assumption that $\varepsilon\tau$ for smoldering embers does not vary with wavelength between red and green. No study to date has examined such variations for smoldering wood.

3. Results

3.1. Stationary embers

For stationary ember tests, the camera *ISO* and *t* were selected for images that were neither too dim nor too bright (i.e., the brightest red pixel value was in the range of 20,000–65,000). Ember images were recorded at 1 Hz.

The stationary ember image temperatures are plotted versus time after ignition in Fig. 2a and b. Most of the scatter in these plots occurs because some embers burn hotter than others. This is attributed to differences in the maple rod morphology and the development of cracks in the ember surface. The image temperatures of most of the embers generally increase with time after ignition, and the mean heating rate for Fig. 2 embers is 0.77 °C/s.

For these data the means are given in Table 1 and shown as horizontal lines in Fig. 2a and b. The mean standard deviation per ember, also shown in Table 1, reflects both the pyrometry repeatability and temporal variations of the embers, including their 0.77 °C/s mean heating rate. For $V_{wind} = 2$ m/s the mean temperature is higher than the mean of 930 °C from Ref. [14] with $V_{wind} = 2.5$ m/s, which is attributed to the lack of multiple embers and images in Ref. [14] and to the larger and better controlled fan used here.

For each ember in Fig. 2a, the mean temperature at all times was found. These are plotted in Fig. 3 with respect to *OID*. A linear regression of these data has an R^2 coefficient of determination of only 0.0003, indicating the most reasonable fit is the horizontal line shown. The scatter in these temperatures is again attributed to how some embers burn hotter than others. Similar behavior was observed for the $V_{wind} = 2$ m/s data of Fig. 2b, but this is not plotted here because there are only 3 embers, and a reduced range of *OIT*.

The temperatures of Fig. 3 were converted to $\varepsilon\tau$ in the visible by applying a relationship established by Ref. [14] for similar embers, namely.

Airborne firebrands were emulated by rotating the camera such that the ember appeared as a streak in the image. The camera was mounted on a shaft connected to a variable-speed motor and aligned with the center of the CMOS sensor. The camera axis of rotation was either horizontal or vertical, producing streaks parallel or perpendicular to the rod, respectively. All streaks were 5472 pixels long. Using an Arduino microprocessor, a distance sensor, and a specified exposure time, the camera exposure began just before the ember entered the field of view and ended soon after it exited. The streaking ember's apparent velocity with respect to the camera, V_{em}, was determined from.

$$V_{em} = \omega \, OID, \qquad (3)$$

where ω is camera angular velocity. The range of V_{em} considered here, see Table 1, spans the terminal velocities for these rods, discussed above. For each streaking ember, the *image temperature* is defined as the mean of the non-null temperatures in the image. The mean of all the streak temperatures for a streaking ember is defined as the *ember temperature*. The standard deviation of the streak temperatures was also found. As summarized in Table 1, 1198 streak images of 40 streaking embers with either horizontal or vertical axis of camera rotation were recorded and analyzed at various *OID*, V_{em}, and V_{wind}.

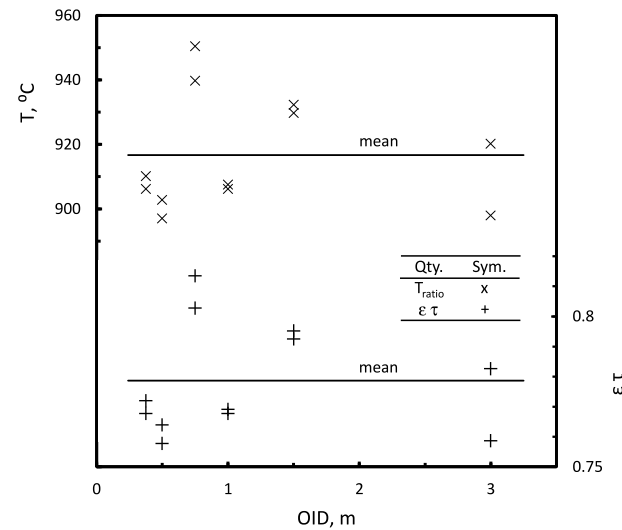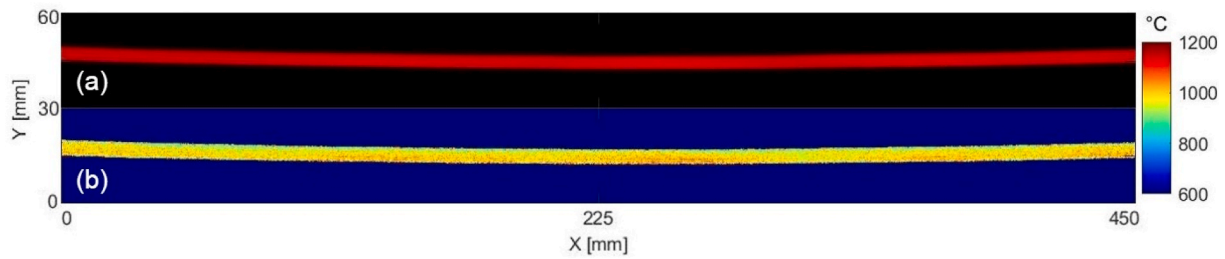**Fig. 4.** (a) A streaking ember image recorded with a vertical axis of camera rotation and (b) its temperature contours. This firebrand was in the view for 450 ms.
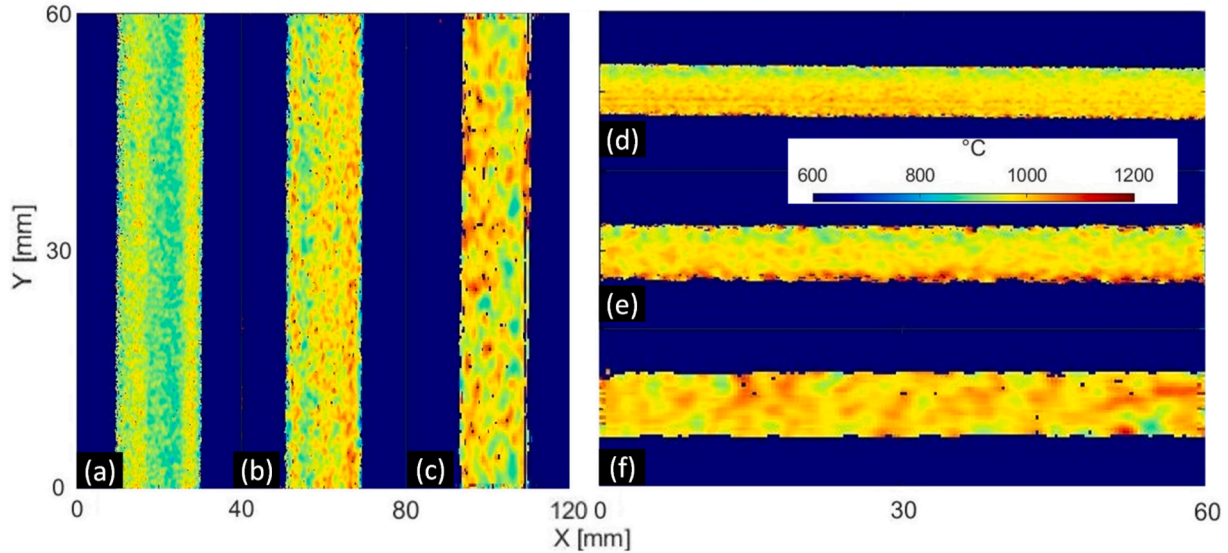

Fig. 5. Temperatures of streaking embers recorded with (a–c) horizontal and (d–f) vertical axes of camera rotation. Only the central part of each streak is shown.

Table 2
Conditions for the streaks of Figs. 4 and 5.

Fig.	OID,m	V_{em},m/s	V_{wind},m/s	ISO	t,ms	T,°C
4	0.375	2	2	64	500	975
5a	0.375	2	2	500	500	923
5b	0.75	4	2	640	500	964
5c	1.5	8	2	640	620	971
5d	0.375	2	2	64	500	975
5e	0.75	8	2	200	250	974
5f	1.5	12	2	100	333	988

$$\varepsilon\,\tau = \exp\left[-\frac{C_2}{\lambda}\left(\frac{\frac{88.6\ K}{T_{ratio}} - 0.0608}{1.06\ T_{ratio} - 88.6\ K}\right)\right], \qquad (4)$$

where $\lambda = 680$ nm. The resulting $\varepsilon\tau$ are plotted with respect to OID in Fig. 3. They have a mean of 0.78 and no significant variation with OID.

3.2. Emulated firebrands

A representative image of a streaking ember recorded with a vertical axis of camera rotation is shown in Fig. 4a, with conditions as shown in Table 2. The streak color and intensity are reasonably uniform. The streak is bowed because the rotation axis was not perfectly vertical. For streaks a third processing step was added whereby the non-null temperatures were smoothed using 7×7 pixel means. A color contour plot of the resulting temperatures is shown in Fig. 4b. These comprise 4×10^5 temperatures with a mean and standard deviation of 975 and 53 °C.

Fig. 5 shows the measured temperature contours for six other streaking embers, with conditions as shown in Table 2. The streak temperatures are similar. An increase in measurement noise with increasing OID is evident in Fig. 5. This arises because fewer pixels are illuminated and the shorter dwell times reduced the luminous energy incident on each CMOS pixel.

Quantity $\varepsilon\tau$ was not determined for the streaking embers, although at each pixel the color ratio temperature, T_{ratio}, can be converted to $\varepsilon\tau$ using Eq. (4). For other fuels or conditions a relationship like Eq. (4) may not be available, in which case one could be found by performing both ratio and grayscale pyrometry on a stationary ember, as in Ref. [14]. Alternatively, if the ember dwell time can be estimated at each pixel in a firebrand streak, grayscale pyrometry can be performed. Quantity $\varepsilon\tau$ can then be found at each pixel using.

$$\varepsilon\,\tau = \exp\left[-\frac{C_2}{\lambda}\left(\frac{1}{T_{gs}} - \frac{1}{T_{ratio}}\right)\right], \qquad (5)$$

where T_{gs} is the temperature obtained with grayscale pyrometry assuming $\varepsilon\tau = 1$.

Pyrometry was performed on 1198 streaking embers for various wind velocities, OID, ember velocities, and axes of rotation (see Ref. [25] for details). The streak temperatures were averaged over time for each streaking ember. Fig. 6a and b shows the resulting streaking ember temperatures for $V_{wind} = 1$ and 2 m/s, respectively. Also plotted are the stationary ember temperatures (averaged over time). The mean temperatures of the data in Fig. 6a and b, shown with horizontal lines, are 918 and 955 °C, respectively. For these conditions, linear regression analyses find that neither OID nor V_{em} has a statistically significant effect on the measured temperatures. As seen in Table 1 and Fig. 6, the ember
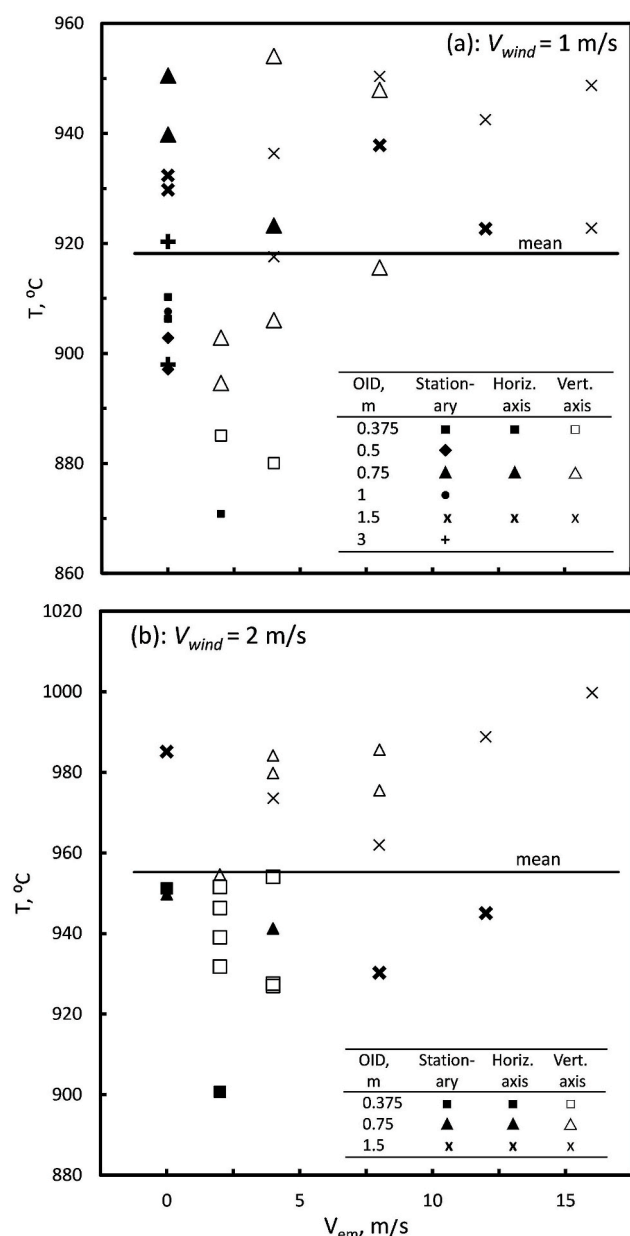
Fig. 6. Stationary and streaking ember temperature versus ember velocity for (a) 31 embers with V_{wind} = 1 m/s and (b) 24 embers with V_{wind} = 2 m/s. Each point represents one ember, averaged over all its recorded times.

temperatures measured three ways – with no camera rotation, horizontal axis rotation, and vertical axis rotation – were not statistically different.

While stationary embers benefit from increased luminous energy at each pixel, streaking embers benefit from illuminating more pixels. The net effect is that the measurement accuracy of the ember temperatures is nearly the same for stationary and streaking embers. These observations are supported by the data of Table 1, which show that the mean ember temperatures and standard deviations are similar for stationary and streaking embers.

Some limitations of color ratio pyrometry for firebrands, which may require addressing before its use in real fires, are that it has not been demonstrated for distances greater than 3 m, for embers out of the focal plane, for embers illuminated by ambient light, or for tumbling embers.

4. Conclusions

Color ratio pyrometry of tethered and smoldering wood embers was performed with a digital color camera that had been calibrated with a blackbody furnace. Airborne firebrands were emulated by rotating the camera during exposures to produce streak images. Over 1600 images of 15 stationary embers and 40 streaking embers were analyzed to quantify the effects of time after ignition, wind velocity, ember velocity and distance, and camera axis of rotation. The key findings are as follows.

1. Airborne firebrands can be emulated by rotating a camera. The resulting streak images are identical to those that would result from a nontumbling airborne firebrand with the same temperature, distance, and velocity. Emulated firebrands are attractive for pyrometry because their temperatures can be independently verified.
2. The same mean temperatures were measured for stationary and streaking embers. These were 918 and 955 °C for 1 and 2 m/s wind velocities, respectively.
3. The measured temperatures did not vary significantly with ember distance or velocity, or with camera axis of rotation. However, the embers generally grew hotter with time, with a mean heating rate of 0.77 °C/s.
4. The pyrometry accuracy is similar for stationary and streaking embers.

CRediT author statement

James Baldwin: Data curation, Formal analysis, Investigation, Methodology, Software, Writing- Original draft preparation. Peter Sunderland: Conceptualization, Funding acquisition, Project administration, Writing – reviewing and editing.

Declaration of competing interest

The authors declare that they have no known competing financial interests or personal relationships that could have appeared to influence the work reported in this paper.

Data availability

Data will be made available on request.

References

[1] J.D. Cohen, Preventing disaster: home ignitability in the wildland urban interface, J. For. 98 (2000) 15–21.
[2] W.E. Mell, S.L. Manzello, A. Maranghides, D. Butry, R.G. Rehm, The wildland-urban interface fire problem – current approaches and research needs, Int. J. Wildland Fire 19 (2010) 238–251, https://doi.org/10.1071/WF07131.
[3] A. Sharifian, J. Hashempour, A novel ember shower simulator for assessing performance of low porosity screens at high wind speeds against firebrand attacks, J. Fire Sci. 34 (2016) 335–355, https://doi.org/10.1177/073490411665517.
[4] A.C. Fernandez-Pello, Wildland fire spot ignition by sparks and firebrands, Fire Saf. J. 91 (2017) 2–10.
[5] S.L. Manzello, S. Suzuki, M.J. Gollner, A.C. Fernandez-Pello, Role of firebrand combustion in large outdoor fire spread, Prog. Energy Combust. Sci. 76 (2020), https://doi.org/10.1016/j.pecs.2019.100801.
[6] S.E. Caton, R.S.P. Hakes, M.J. Gollner, D.J. Gorham, A. Zhou, Review of pathways for building fire spread in the wildland urban interface part I: exposure conditions, Fire Technol. 53 (2017) 429–473, https://doi.org/10.1007/s10694-016-0589-z.
[7] Y.M. Abul-Huda, N. Bouvet, Thermal dynamics of deposited firebrands using phosphor thermometry, Proc. Combust. Inst. 38 (2021) 4757–4765, https://doi.org/10.1016/j.proci.2020.07.098.

[8] C.S. Tarifa, P.P. Del Notario, F.G. Moreno, On the flight paths and lifetimes of burning particles of wood, Proc. Combust. Inst. 10 (1965) 1021–1037, https://doi.org/10.1016/S0082-0784(65)80244-2.

[9] R.A. Anthenien, S.D. Tse, A.C. Fernandez-Pello, On the trajectories of embers initially elevated or lofted by small scale ground fire plumes in high winds, Fire Saf. J. 41 (2006) 349–363, https://doi.org/10.1016/j.firesaf.2006.01.005, doi:.

[10] S.L. Manzello, S. Park, T.G. Cleary, Investigation on the ability of glowing firebrands deposited within crevices to ignite common building materials, Fire Saf. J. 44 (2009) 894–900, https://doi.org/10.1016/j.firesaf.2009.05.001.

[11] E. Koo, P.J. Pagni, D.R. Weise, J.P. Woycheese, Firebrands and spotting ignition in large-scale fires, Int. J. Wildland Fire 19 (2010) 818–843, https://doi.org/10.1071/WF07119.

[12] A. Tohidi, N. Kaye, W. Bridges, Statistical description of firebrand size and shape distribution from coniferous trees for use in Metropolis Monte Carlo simulations of firebrand flight distance, Fire Saf. J. 77 (2015) 21–35, https://doi.org/10.1016/j.firesaf.2015.07.008.

[13] J. Urbas, W.J. Parker, G.E. Luebbers, Surface temperature measurements on burning materials using an infrared pyrometer: accounting for emissivity and reflection of external radiation, Fire Matls 28 (2004) 33–53, https://doi.org/10.1002/fam.844.

[14] D.K. Kim, P.B. Sunderland, Fire ember pyrometry using a color camera, Fire Saf. J. 106 (2019) 88–93, https://doi.org/10.1016/j.firesaf.2019.04.006, doi:.

[15] J.L. Urban, A.C. Fernandez-Pello, M. Vicariotto, D. Dunn-Rankin, Temperature measurement of glowing embers with color pyrometry, Fire Technol. 55 (2019) 1013–1026, https://doi.org/10.1007/s10694-018-0810-3.

[16] V. Fateev, M. Agafontsev, S. Volkov, A. Filkov, Determination of smoldering time and thermal characteristics of firebrands under laboratory conditions, Fire Saf. J. 91 (2017) 791–799, https://doi.org/10.1016/j.firesaf.2017.03.080, doi:.

[17] C. He, K. Liu, L. Shu, X. Hong, S. Zhang, The diagnostic methods for resurgences of smoldering fire in the forests by infrared thermal imaging, Spectrosc. Spectr. Anal. 38 (2018) 326–332, https://doi.org/10.3964/j.issn.1000-0593(2018)01-0326-07.

[18] H. Lu, L. Ip, A. Mackrory, L. Werrett, J. Scott, D. Tree, L. Baxter, Particle surface temperature measurements with multicolor band pyrometry, AIChE J. 55 (2009) 243–255, https://doi.org/10.1002/aic.11677.

[19] Y. Liu, J.L. Urban, C. Xu, C. Fernandez-Pello, Temperature and motion tracking of metal spark sprays, Fire Technol. 55 (2019) 2143–2169, https://doi.org/10.1007/s10694-019-00847-3.

[20] H. Guo, J.A. Castillo, P.B. Sunderland, Digital camera measurements of soot temperature and soot volume fraction in axisymmetric flames, Appl. Opt. 52 (2013) 8040–8047, https://doi.org/10.1364/AO.52.008040.

[21] P. Toth, T. Draper, A.B. Palotas, T.A. Ring, E.G. Eddings, Three-dimensional combined pyrometric sizing and velocimetry of combusting coal particles II: pyrometry, Appl. Opt. 54 (2015) 4916–4926, https://doi.org/10.1364/AO.54.004916.

[22] S. Prohanov, A. Filkov, D. Kasymov, M. Agafontsev, V. Reyno, Determination of firebrand characteristics using thermal videos, Fire 3 (2020) 68, https://doi.org/10.3390/fire3040068.

[23] J. Gabitto, C. Tsouris, Drag coefficient and settling velocity for particles of cylindrical shape, Powder Technol. 183 (2018) 314–322, https://doi.org/10.1016/j.powtec.2007.07.031.

[24] D. Coffin, Decoding raw digital photos in Linux. https://www.dechifro.org/dcraw/.

[25] J.H. Baldwin, Imaging Pyrometry of Wood Embers under Simulated Movement, MS Thesis, University of Maryland, College Park, MD, 2022.

[26] K. Decker, Imaging Pyrometry of Smoldering Wood Embers at Various Distances and Illuminations, MS Thesis, University of Maryland, College Park, MD, 2020.